RESEARCH ARTICLE

Integrated intravoxel incoherent motion tensor and diffusion tensor brain MRI in a single fast acquisition

Olaf Dietrich[1] | Mengfei Cai[2] | Anil Man Tuladhar[2] | Mina A. Jacob[2] |
Gerald S. Drenthen[3] | Jacobus F. A. Jansen[3,4] | José P. Marques[2] |
Johanna Topalis[1] | Michael Ingrisch[1] | Jens Ricke[1] | Frank-Erik de Leeuw[2] |
Marco Duering[5] | Walter H. Backes[3]

[1]Department of Radiology, University Hospital, LMU Munich, Munich, Germany

[2]Department of Neurology, Donders Center for Medical Neurosciences, Radboud University Medical Center, Nijmegen, The Netherlands

[3]Schools for Mental Health and Neuroscience (MHeNs) and Cardiovascular Diseases (CARIM), Department of Radiology and Nuclear Medicine, Maastricht University Medical Center, Maastricht, The Netherlands

[4]Department of Electrical Engineering, Eindhoven University of Technology, Eindhoven, The Netherlands

[5]Medical Image Analysis Center (MIAC AG) and qbig, Department of Biomedical Engineering, University of Basel, Basel, Switzerland

Correspondence
Prof. Dr. rer. nat. Olaf Dietrich, Department of Radiology, University Hospital, LMU Munich, Marchioninistr. 15, 81377 Munich, Germany.
Email: od@dtrx.net

The acquisition of intravoxel incoherent motion (IVIM) data and diffusion tensor imaging (DTI) data from the brain can be integrated into a single measurement, which offers the possibility to determine orientation-dependent (tensorial) perfusion parameters in addition to established IVIM and DTI parameters. The purpose of this study was to evaluate the feasibility of such a protocol with a clinically feasible scan time below 6 min and to use a model-selection approach to find a set of DTI and IVIM tensor parameters that most adequately describes the acquired data. Diffusion-weighted images of the brain were acquired at 3 T in 20 elderly participants with cerebral small vessel disease using a multiband echoplanar imaging sequence with 15 b-values between 0 and 1000 s/mm^2 and six non-collinear diffusion gradient directions for each b-value. Seven different IVIM-diffusion models with 4 to 14 parameters were implemented, which modeled diffusion and pseudo-diffusion as scalar or tensor quantities. The models were compared with respect to their fitting performance based on the goodness of fit (sum of squared fit residuals, chi^2) and their Akaike weights (calculated from the corrected Akaike information criterion). Lowest chi^2 values were found using the model with the largest number of model parameters. However, significantly highest Akaike weights indicating the most appropriate models for the acquired data were found with a nine-parameter IVIM–DTI model (with isotropic perfusion modeling) in normal-appearing white matter (NAWM), and with an 11-parameter model (IVIM–DTI with additional pseudo-diffusion anisotropy) in white matter with hyperintensities (WMH) and in gray matter (GM). The latter model allowed for the additional calculation of the fractional anisotropy of the pseudo-diffusion tensor (with a median value of 0.45 in NAWM, 0.23 in WMH, and 0.36 in GM), which is not accessible with the usually performed IVIM acquisitions based on three orthogonal diffusion-gradient directions.

1 | INTRODUCTION

Diffusion-weighted MRI is a well established imaging technique that is sensitive to incoherent motion of spins caused by their thermal energy ("Brownian motion") and, in vivo, also to incoherent motion caused by pseudo-random flow.[1,2] A particularly important variant of diffusion-weighted MRI in the brain is diffusion tensor imaging (DTI), which can quantify the mobility of water molecules along different spatial orientations, thus detecting the geometry and integrity of white-matter fiber bundles.[3,4] DTI requires the acquisition of a number of diffusion-weighted images (at least six, but frequently many more) with different spatial diffusion-gradient orientations.[5,6] Typically, for the brain parenchyma, intermediate to high diffusion weightings ($b \gtrsim 1000$ s/mm^2) are used. The diffusion tensor calculated from these data is a symmetric 3×3 matrix with six independent entries that describe the orientation-dependent diffusion properties.

A different, emerging application of diffusion-weighted MRI exploits the aforementioned sensitivity of the diffusion-weighted signal to pseudo-random microscopic flow ("pseudo-diffusion"), which is mainly associated with capillary blood flow (i.e., perfusion), but can also be caused by other physiological processes.[7] This contrast mechanism is today referred to as the intravoxel incoherent motion (IVIM) effect. The IVIM contrast has been used in recent years for an increasing number of applications, predominantly in oncological studies.[8–10] IVIM MRI is based on the acquisition of additional diffusion-weighted images at relatively low b-values (between 0 and about 200 s/mm^2) to capture the comparably fast pseudo-diffusion of circulating blood water.[11,12] Typically, any orientation dependence is removed by averaging the signal over three orthogonal orientations, i.e., by acquiring so-called trace images. The different diffusion components can be determined using a biexponential model function for IVIM data analysis, from which two additional parameters (perfusion volume fraction, f, and pseudo-diffusion coefficient, D^*) are calculated, complementing the conventional diffusion coefficient (parenchymal diffusivity of water, D).[1] Since bi-exponential analysis is generally very sensitive to noise,[13] multiple repetitions of these acquisitions are typically averaged to obtain sufficiently large signal-to-noise ratios and parameter fitting is frequently performed in a two-step approach.[14]

Typically, diffusion-weighted MRI protocols are optimized for a single application, either to distinguish the small IVIM effect from the parenchymal diffusion signal or to quantify the anisotropic properties of parenchymal diffusion with DTI. However, it is also possible (but rarely done) to combine IVIM and DTI acquisitions, which requires the acquisition of multiple different b-values (including several low b-values) each acquired with at least six non-collinear diffusion-gradient orientations. Only such a dataset allows for a combined IVIM tensor/diffusion tensor evaluation, which can take into account orientation dependence not only in the conventional DTI analysis, but also in the (now tensor-aware) IVIM analysis.[15–17] The latter strategy allows for a multitude of different signal models, in which, e.g., the pseudo-diffusion coefficient can be described as a tensor resulting in a large number of free model parameters (e.g., 14 parameters for two tensors, the perfusion fraction, and the signal scaling). It depends on the underlying microstructure and physiology of the tissue, but also on the signal-to-noise ratio of the acquired data if fitting such a large number of parameters is feasible and results in biologically meaningful parameter maps.

A cerebral pathology that appears highly suitable for the evaluation of the combined IVIM–DTI analysis is cerebral small vessel disease (cSVD).[18,19] cSVD is characterized by alterations in brain parenchyma such as white matter with hyperintensities (WMH), lacunes, and microbleeds.[20–22] An increasing number of studies suggest that chronic cerebral hypoperfusion is involved in the etiology of cSVD,[23–26] while evidence from DTI-based studies demonstrates loss of microstructural integrity of the WM in cSVD.[27] Therefore, cSVD can serve as a suitable disorder for the simultaneous assessment of perfusion and diffusion changes by an integrated IVIM–DTI acquisition. Previous studies using scalar IVIM models have already shown distinct pathophysiological effects in patients with cSVD and neurodegenerative Alzheimer's disease.[28,29]

The purpose of this study was to evaluate such an integrated IVIM–DTI acquisition of the brain with a clinically feasible scan time below 6 min and to use a model-selection approach to find a set of DTI and IVIM tensor parameters that most adequately describes the acquired data.

2 | MATERIAL AND METHODS

2.1 | Study population

The MRI data used in the present study are a subset of the ongoing longitudinal Radboud University Nijmegen Diffusion Tensor and Magnetic Resonance Cohort (RUN DMC) with baseline assessment in 2006 and follow up in 2011, 2015, and 2020; details of this cohort can be found in the articles by van Leijsen et al. and Cai et al.[30,31] IVIM data ($n = 231$) were available in the follow-up scans in 2020. To evaluate the potential of an integrated IVIM–DTI acquisition in normal-appearing tissue and in microstructural abnormalities, we randomly selected 20 participants with a

wide range of WMH burden (median [interquartile range] 20.29 mL [14.70 mL, 30.40 mL], range 0.75–66.9 mL). The mean age was 77.0 years (standard deviation 7.96 years), and 13 participants (65%) were males. The Arnhem-Nijmegen Region Medical Review Ethics Committee approved the study and all participants provided written informed consent.

2.2 | Image acquisition

All MRI data were acquired on a 3 T MRI system (Magnetom Prisma, Siemens Healthineers, Erlangen, Germany) using a 32-channel head coil (Siemens Healthineers). The maximum gradient amplitude of the MRI system was 80 mT/m with a slew rate of 200 T/m/s.

Integrated IVIM and DTI diffusion-weighted images were acquired with six diffusion-gradient orientations, $\mathbf{g}$ ($\mathbf{g} = (1,0,1), (−1,0,1), (0,1,1),$ $(0,1,−1), (1,1,0), (−1,1,0)$ in the magnet coordinate system) and 15 (nominal) b-vales: $b = 0, 5, 10, 15, 20, 30, 40, 50, 60, 100, 200, 400, 600,$ $800, 1000$ s/mm^2, resulting in a total of 90 measurements ($b = 0$ s/mm^2 was repeated six times). Measurements were made using a fat-saturated single-shot spin-echo multiband echoplanar-imaging sequence[32–34] with an echo time (T_E) of 60.6 ms, a repetition time (T_R) of 3210 ms, and a receiver bandwidth of 2245 Hz/pixel. The cubic voxel dimensions were $2 \times 2 \times 2$ mm^3 in a field of view of 212×212 mm^2; the number of (axial) slices was 70. Data were acquired with a parallel imaging acceleration factor of 2 and a multiband acceleration factor of 2; the total acquisition time was 5 min 21 s. An additional $b = 0$ s/mm^2 scan with identical acquisition parameters, but reversed phase-encoding direction, was acquired for subsequent distortion correction.

For anatomical reference and segmentation, magnetization-prepared two rapid-acquisition gradient-echoes (MP2RAGE) MRI ($T_R = 5500$ ms, $T_E = 3.84$ ms, $T_{I1}/T_{I2} = 700/2500$ ms, 0.85 mm isotropic voxel size) and, for segmentation of WMH, fluid-attenuated inversion recovery (FLAIR) ($T_R = 5000$ ms, $T_E = 394$ ms, $T_I = 1800$ ms, 0.85 mm isotropic voxel size) images were acquired.

2.3 | Data processing and segmentation

MP2RAGE images were post-processed to obtain high-contrast 3D T_1-weighted (so-called regularized UNI) images exhibiting the best compromise between a significant decrease in noise levels in regions of low or no signal (near air or skull) and a small increase in image intensity bias[35] using freely available code (https://github.com/JosePMarques/MP2RAGE-related-scripts). WMH was segmented from coregistered and bias-corrected T_1-weighted and FLAIR images by using a variant of the 3D U-net deep learning algorithm.[36] All WMH segmentations were then manually edited and cleaned from misclassified artifacts using a custom 3D editing tool written in MATLAB (R2018a, MathWorks, Natick, MA, USA).

Gray matter (GM), white matter (WM), and cerebrospinal fluid (CSF) probability maps were segmented from T_1-weighted images using SPM12 (http://www.fil.ion.ucl.ac.uk/spm/). Additionally, we used manually corrected WMH masks to refine the initial, automatically segmented probability maps[21] and to obtain normal-appearing white matter (NAWM) masks (by removing the WMH voxels from the original WM mask). To restrict the subsequent analysis to the cerebrum, we excluded the cerebellum and brain stem from all masks. This was done by, first, calculating cerebellum and brain stem masks with Sequence Adaptive Multimodal Segmentation (SAMSEG)[37] and then removing all cerebellum and brain stem voxels from the GM, WM, and CSF probability maps. Finally, we registered the obtained GM, WM, and CSF probability maps into IVIM space using ANTs[38] and minimized the influence of partial-volume effects by choosing only voxels for each mask with tissue probabilities greater than 0.99. Examples of the resulting masks for one participant are shown in Figure 1.

IVIM–DTI data were pre-processed before further evaluation with a standard pipeline including MRtrix dwidenoise, MRtrix mrdegibbs,[39] and FSL TOPUP distortion correction,[40] as well as eddy-current and motion correction (FSL eddy_correct).[41]

2.4 | IVIM and DTI evaluation

For model comparison and quantitative evaluation, we considered seven different IVIM–DTI models with varying numbers of free parameters that can all be considered as special cases of the following, most general model used in our study:

$$S(b,\mathbf{g}) = S_0 \left((1-f) \exp\left(-b\,\mathbf{g}^T \mathbf{D} \mathbf{g}\right) + f \exp\left(-b\,\mathbf{g}^T \mathbf{D}^* \mathbf{g}\right) \right). \tag{1}$$

This model is based on a symmetric 3×3 diffusion tensor, $\mathbf{D}$ (in equations, vectors and tensors are denoted by bold letters), describing anisotropic parenchymal water diffusion, a symmetric 3×3 pseudo-diffusion tensor, $\mathbf{D}^*$, describing anisotropic capillary flow, and a scalar perfusion signal fraction, f. Each of the tensors has six free parameters ($D_{xx}, D_{yy}, D_{zz}, D_{xy}, D_{xz}, D_{yz}; D_{xx}^*, D_{yy}^*, D_{zz}^*, D_{xy}^*, D_{xz}^*, D_{yz}^*$), so together with the signal scaling, S_0, and the perfusion fraction, f, this model has $p = 14$ free fit parameters. When naming specific models, we denote the above-mentioned
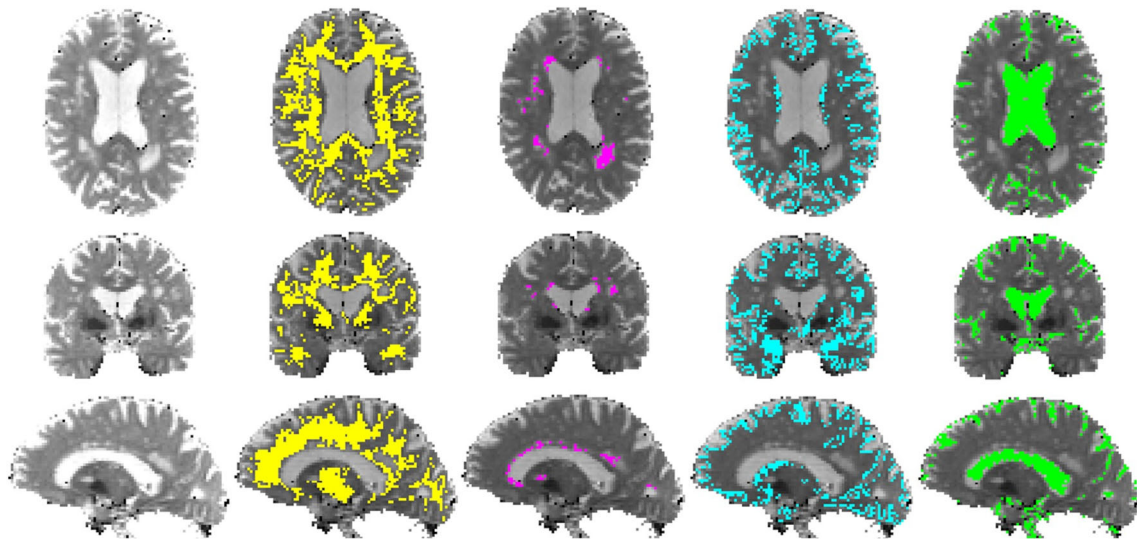
FIGURE 1 Brain segmentations determined from tissue probability maps: from left to right, b_0 images, NAWM region (yellow), WMH region (magenta), GM region (cyan), and CSF region (green). To minimize partial-volume effects, the threshold for tissue selection was set to a probability of 99%, which mostly excluded voxels with contributions from more than one tissue (and resulted in relatively sparse voxel masks).

tensors by "D_6" and "D_6*" to differentiate from the scalar parameters "D" and "D^*". So, the model in Equation (1) is referred to as "D_6*–f–D_6" ($p = 14$). In contrast, the usually used (scalar) IVIM model[1]

$$S(b) = S_0 \left((1-f) \exp(-b\,D) + f \exp(-b\,D^*) \right) \tag{2}$$

has $p = 4$ parameters and is denoted by "D^*–f–D". The standard (non-IVIM) DTI model

$$S(b, \mathbf{g}) = S_0 \exp(-b\mathbf{g}^{\mathsf{T}}\mathbf{D}\mathbf{g}) \tag{3}$$

with $p = 7$ parameters is denoted by "D_6" ($p = 7$). All investigated tensor models (i.e., all models except D^*–f–D, Equation 2) included a tensor description (D_6) of the parenchymal diffusion, as the pertaining signal decay is much stronger than for the IVIM part.

The simplest combination of D^*–f–D and D_6 is the IVIM model D^*–f–D_6 with scalar IVIM parameters, D^* and f, and a diffusion tensor, $\mathbf{D}$, resulting in $p = 9$ free parameters, given by

$$S(b, \mathbf{g}) = S_0 \left((1-f) \exp(-b\mathbf{g}^{\mathsf{T}}\mathbf{D}\mathbf{g}) + f \exp(-bD^*) \right). \tag{4}$$

All other evaluated models were derived from Equation (1) by restricting the tensorial properties of $\mathbf{D}^*$ to reduce the number of IVIM parameters from six (full tensor, $\mathbf{D}^*$), while retaining the seven parameters of S_0 and $\mathbf{D}$. This approach was motivated by the higher robustness of the measured diffusion-tensor parameters compared with pseudo-diffusion tensor components, and is independent of any biological assumptions about the underlying tissue structure.

The strongest applied restriction of the general 14-parameter model D_6*–f–D_6 is to assume that $\mathbf{D}^*$ is a tensor proportional to the $\mathbf{D}$ tensor, thus having the same anisotropy and orientation as $\mathbf{D}$. Hence, instead of fitting $\mathbf{D}^*$ based on six free parameters as in Equation (1), it can be defined as a scaled normalized $\mathbf{D}$ tensor. To do this, we first determine the normalized $\mathbf{D}$ tensor with trace 3: $\hat{\mathbf{D}} = \mathbf{D} / \left(\frac{1}{3} \mathrm{tr}\,\mathbf{D} \right)$. Now we set $\mathbf{D}^* = D^* \hat{\mathbf{D}}$ with the scalar scaling factors D^*. This perfusion-signal model is denoted "D_6*s" (letter "s" for "scaled") and can be integrated into the IVIM model D^*–f–D_6, yielding "D_6*s–f–D_6". This model has $p = 9$ parameters (the same number of parameters as the D^*–f–D_6 model with isotropic IVIM properties).

In a next step, to allow for different degrees of anisotropy, $\mathbf{D}^*$ can be defined as a linear combination of a normalized isotropic tensor, $\mathbf{1}$, and the normalized tensor $\hat{\mathbf{D}}$ from above. The weighting of these two components is given by the "anisotropy" coefficients $(1 - a)$ and a: if $\mathbf{D}^*$ is defined as $\mathbf{D}^* = D^* \left((1-a)\mathbf{1} + a\hat{\mathbf{D}} \right)$, the anisotropy of $\mathbf{D}^*$ can be varied by a, between 0 (for $a = 0$) and the anisotropy of $\mathbf{D}$ (for $a = 1$). We denote this perfusion-signal model by "D_6*a" (the letter "a" indicating the anisotropy parameter) and define the model "D_6*a–f–D_6" with 10 free parameters.

Finally, as a last modeling approach with complexity between D_6^*a on the one hand and the full D_6^* model on the other hand, it is possible to allow for arbitrary tensor eigen*values*, while keeping the eigen*vectors* fixed as taken from the diffusion tensor, D. These models can exhibit arbitrary anisotropy values and tensor shapes (e.g., cylindrical or flat), but the spatial orientation of the tensor ellipsoid is the same as the one of the D tensor in each voxel. Mathematically, this model can be described using the (orthogonal) eigenvector matrix E and the diagonal eigenvalue matrix $\Delta = \mathrm{diag}(\lambda_1,\lambda_2,\lambda_3)$ of the diffusion tensor D, which can, thus, be expressed as $D = E\Delta E^\mathsf{T}$. We can now define $D^* = E\,\mathrm{diag}(D_1^*,D_2^*,D_3^*)E^\mathsf{T}$ with three independent eigenvalues but the same eigenvectors as D. We denote this perfusion-signal model by "D_6^*e" (with the letter "e" for eigenvalues) and define the model "$D_6^*e\text{–}f\text{–}D_6$" with 11 free parameters. An overview over all seven models is presented in Table 1; only the last model in this table allows for fully independent IVIM tensor orientations. (10 more IVIM–DTI models that allow for a tensor-valued perfusion fraction f are presented and evaluated in Supporting Information 3.)

For all models with pseudo-diffusion parameters (i.e., all models except D_6), step-wise ("segmented") fitting was used.[14] First, a tissue-diffusion model ("high-b model") was fitted to the signals at $b \geq b_{\mathrm{segm}}$ resulting in either a (scalar) diffusion coefficient, D, or a diffusion tensor, D, describing normal ("slow") tissue diffusion. Then the perfusion components (scalar parameters D^* and f, and/or tensor parameters D^*) were fitted using the given full signal equations with fixed tissue-diffusion parameters. The b-value threshold for segmentation was set to $b_{\mathrm{segm}} = 400$ s/mm^2 in all models (i.e., acquisitions with b-values between 0 and 200 s/mm^2 were excluded for the initial fit). (An additional evaluation performed with $b_{\mathrm{segm}} = 600$ s/mm^2 is discussed in Supporting Information 2.)

Non-linear data fitting (monoexponential model and tensor models) was performed with the non-linear least-squares fit routine "kmpfit" from the Kapteyn package, Version 3.0.[42] The signal models were implemented in Python 3.7.

2.5 | Model comparison and statistical analysis

The fitting performances of the seven different IVIM–DTI signal models ($S_m, m = 1...7$) listed above were compared using the residual sum of squared fit errors (chi^2).

$$\chi^2(m) = \sum_{n=1}^{N=90} \left(S_m(b_n,\mathbf{g}_n) - S_n/S_{0,\mathrm{mean}}\right)^2 \tag{5}$$

where S_n are the measured signal intensities for all $N = 90$ b-values and gradient directions, and $S_{0,\mathrm{mean}}$ is the (voxelwise) mean value of the signal over the six $b = 0$ s/mm^2 measurements (the model parameter S_0 from Equation (1) is still fitted and not assumed to be exactly $S_0 = 1$). Then the (corrected) Akaike information criterion

$$\mathrm{AICc}(m) = N\log\left(\chi^2(m)/N\right) + 2(p+1) + 2(p+1)(p+2)/(N-p-2) \tag{6}$$

(for a model with p parameters) was evaluated for each voxel.[43–45]

For each participant, the median values of chi^2 and the AICc were calculated separately for voxels of NAWM, WMH, and GM. Median values were used because of the asymmetric (non-normal) statistical distribution of chi^2 and AICc values. From these individual median values, the corresponding Akaike weights $w(m)$ were calculated as

$$w(m) = \exp\left(-\frac{\Delta(m)}{2}\right) \bigg/ \sum_{m=1}^{7} \exp\left(-\frac{\Delta(m)}{2}\right)$$

TABLE 1 All seven evaluated IVIM–DTI signal models (overview)

Model name	No of fit parameters ("$S_0 + D^* + f + D$")	(Tissue) diffusion	(Perfusion) pseudo-diffusion parameters ($\hat{D}$ and E taken from DTI (high-b) component)
$D^*\text{–}f\text{–}D$	$4 = 1 + 1 + 1 + 1$	D (scalar)	D^*, f
D_6	$7 = 1 + 0 + 0 + 6$	D (tensor)	(none)
$D^*\text{–}f\text{–}D_6$	$9 = 1 + 1 + 1 + 6$	D	D^*, f
$D_6^*s\text{–}f\text{–}D_6$	$9 = 1 + 1 + 1 + 6$	$D\;(=D\hat{D})$	$D^*\hat{D}, f$
$D_6^*a\text{–}f\text{–}D_6$	$10 = 1 + 2 + 1 + 6$	$D\;(=D\hat{D})$	$D^*\left((1-a)\mathbf{1}+a\hat{D}\right), f$
$D_6^*e\text{–}f\text{–}D_6$	$11 = 1 + 3 + 1 + 6$	$D\;(=E\Delta E^\mathsf{T})$	$E\,\mathrm{diag}(D_1^*,D_2^*,D_3^*)E^\mathsf{T}, f$
$D_6^*\text{–}f\text{–}D_6$	$14 = 1 + 6 + 1 + 6$	D	$D_{xx}^*, D_{yy}^*, D_{zz}^*, D_{xy}^*, D_{xz}^*, D_{yz}^*, f$

with $\Delta(m) = \text{AICc}(m) - \min_m \text{AICc}(m)$; the Akaike weight $w(m)$ describes the probability that model m is the best model of all considered models.[44] (Arithmetic) mean values over all participants and standard deviations were determined for each model and used for visual comparison. A linear regression model was used to test if the model with the highest Akaike weight (reference model) had a significantly higher Akaike weight than the other models.[46] Briefly, the dependent variable "Akaike weight" was modeled with the IVIM–DTI model as a single predictor (R pseudo-code: "*lm (Akaike weight ~ relevel(model, ref = best_model)*"). R (Version 4.0.4, The R Foundation, Vienna, Austria) was used for statistical analysis.

2.6 | Quantitative IVIM–DTI evaluation

Using the AICc-optimal IVIM–DTI models (models with the highest Akaike weights), the quantitative fit parameters (e.g., trace of the diffusion tensor, fractional anisotropy (FA), and IVIM perfusion fraction) were collected per voxel in all participants and median values were determined over the individual tissue masks. Then, these individual median results were summarized by calculation of median values and interquartile ranges (distance from first to third quartile) over all participants. In both cases (within each tissue class and over the 20 participants), calculation of the median values was performed to account for non-normally distributed values.

3 | RESULTS

The fit residuals chi^2 (mean values over individual median values of all 20 participants) of the seven evaluated IVIM models are summarized in Figure 2 for NAWM, WMH, and GM separately; individual median values (over all voxels) of chi^2 for each participant are provided in Tables S1.1 to S1.3 in Supporting Information 1. The tensor-free (scalar) model D^*–f–D had by far the highest (i.e. worst) chi^2 values, and all other (i.e. tensor) models had substantially lower chi^2 values for all tissue regions, especially in NAWM and WMH. Differences between the various tensor models were much smaller. The lowest chi^2 value was found for the D_6^*–f–D_6 model, which had the largest number ($p = 14$) of fit parameters. The second lowest chi^2 value was obtained for the D_6^*e–f–D_6 model with $p = 11$ parameters. These results were consistently found for all participants and all tissue regions (except for the two smallest WMH regions), as indicated by the color-coding in Tables S1.1 to S1.3.

The results of the comparison of the seven IVIM models based on the Akaike weights (mean values of all 20 participants) are summarized in Figure 3 for NAWM, WMH, and GM separately. Individual Akaike weights of each participant for these regions are provided in Tables S1.4 to S1.6. The tensor-free model D^*–f–D had the worst (i.e. lowest) weight, while all tensor models were substantially better. In NAWM, the highest (i.e., best) Akaike weight was obtained for the nine-parameter tensor model D^*–f–D_6; all other models yielded significantly smaller Akaike weights ($p < 0.0001$). In WMH and in GM, the 11-parameter model D_6^*e–f–D_6 had the highest Akaike weight; all other models were significantly lower ($p < 0.0001$). This model is at Rank 3 in NAWM with still about half the Akaike weight (18% versus 36%) of the favored model. The color-coding in Tables S1.4 to S1.6 demonstrates that these results were consistently found for NAWM in all participants. In WMH, D_6^*e–f–D_6 showed the highest Akaike weight in 17 of 20 participants; in GM, the same model showed highest weights in 18 of 20 participants.

Based on these results, our further analyses focused on the nine-parameter IVIM–DTI model D^*–f–D_6 as the best model in NAWM and, in particular, on the 11-parameter IVIM–DTI model D_6^*e–f–D_6 as the best model in WMH and GM, which also performed well in WM. For model comparison, we also present results from the traditional tensor-free (scalar) four-parameter IVIM model D^*–f–D and the 14-parameter model
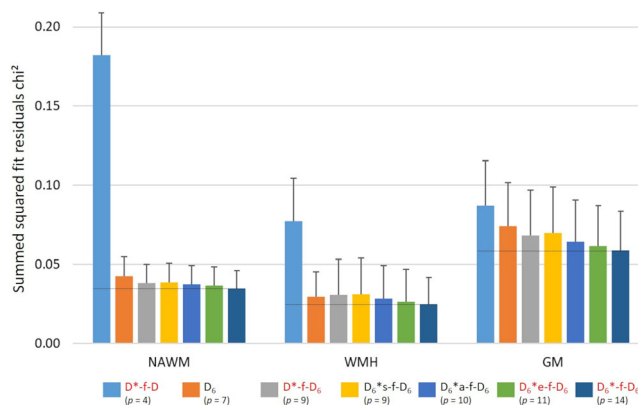

FIGURE 2 Summed squared fit residuals chi^2 (mean values and standard deviations over individual median values of all 20 participants) of the seven IVIM models in NAWM, WMH, and GM; best-fitting models have the lowest chi^2 values within each tissue region (indicated by the dashed horizontal black line topping the D_6^*–f_6–D_6 model). Models used for further analysis are labeled in red.
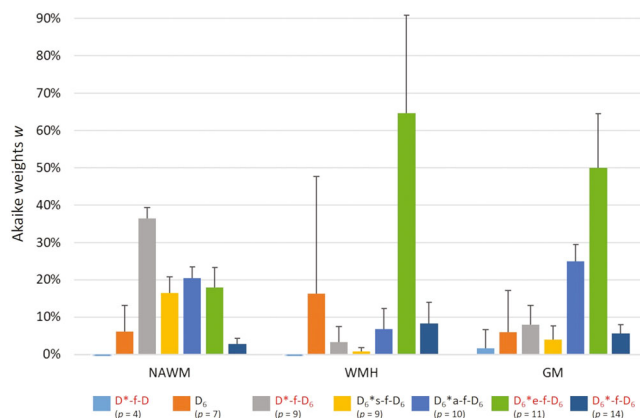
FIGURE 3 AICc-based model comparison (mean values and standard deviations of Akaike weights of all 20 participants) for the seven IVIM models in three brain regions (NAWM, WMH, GM); preferred models have the highest Akaike weights within each tissue region (indicating their probability to be the best of all considered models). Models used for further analysis are labeled in red.

D_6^*–f–D_6. A visual comparison of the parameter maps determined with these four IVIM models in two different brain slices is presented in Figure 4. The tissue-diffusion parameters (D and FA(D)) correspond well to the brain anatomy. The IVIM parameters, f and D^*, show relatively homogeneous parameter distributions with slightly higher noise contributions. The first three models result in visually very similar maps, while the 14-parameter model has globally higher D^* values. Anisotropies of D^* that are independent of the FA of the diffusion tensor can only be obtained for the last two models. The values of FA(D^*) obtained with the 11-parameter model D_6^*e–f–D_6 appear substantially lower than the values of FA(D^*) from the 14-parameter model D_6^*–f–D_6.

The models D^*–f–D_6 ($p = 9$) and D_6^*e–f–D_6 ($p = 11$), favored by the Akaike criterion, were then used to derive quantitative diffusion and perfusion (IVIM) parameters from all 20 participants and to compare these results with parameters from the traditional non-tensor IVIM analysis (D^*–f–D) with $p = 4$ free parameters. The results are summarized as boxplots in Figure 5; the corresponding median values and interquartile ranges are given in Table 2. These three models provided highly consistent diffusion coefficients of approximately 0.75×10^{-3} mm^2/s in NAWM, 1.2×10^{-3} mm^2/s in WMH, and 0.76×10^{-3} mm^2/s in GM as well as fractional diffusion-tensor anisotropy values of approximately 0.46, 0.24, and 0.19, respectively.[*] The pseudo-diffusion coefficient was (depending on the model) between 4.6 and 5.1×10^{-3} mm^2/s in NAWM, between 4.3 and 4.7×10^{-3} mm^2/s in WMH, and between 5.4 and 6.2×10^{-3} mm^2/s in GM. The median of the perfusion fraction was between 6.5 and 7.2% in NAWM, between 7.5 and 10.0% in WMH, and between 5.7 and 8.1% in GM. The perfusion fraction f was systematically lowest with the nine-parameter model D^*–f–D_6; a similar trend (to a lower degree) was also seen for the pseudo-diffusion coefficient, D^*. The FA (boxplots in Figure 6) of the diffusion tensor and of the pseudo-diffusion tensor were approximately 0.46 and 0.45 in NAWM, 0.24 and 0.23 in WMH, and 0.19 and 0.36 in GM, respectively.

Maps of the FA of the pseudo-diffusion tensor, FA(D^*), calculated with the model D_6^*e–f–D_6 are presented in Figure 7. The maps are substantially noisier than the FA maps of the parenchymal diffusion tensor; several voxels show unrealistically high FA(D^*) values. However, over larger areas of the brain (arrow heads), the values of FA(D^*) are distributed smoothly and WMH (that appear hyperintense in the D maps, arrows) show consistently low values of FA(D^*).

4 | DISCUSSION

In this study, we have demonstrated that data from a single time-efficient integrated IVIM–DTI measurement with a cubic voxel size of $2 \times 2 \times 2$ mm^3 and a scan time below 6 min was most adequately described (in terms of the AICc) by extended IVIM models with a tensor description of parenchymal diffusion. As expected, it was shown that such a model with a tensor description of the parenchymal diffusion describes the diffusion decay curves substantially better than tensor-free (scalar) models. In addition, models that allow for carefully restricted pseudo-diffusion (D^* tensor) anisotropy were most adequate in WMH and GM. A more general IVIM model with a full pseudo-diffusion tensor was disfavored by the AICc analysis. These results were obtained from an integrated IVIM–DTI brain MRI protocol with 15 b-values and six diffusion directions for each b-value and comparative computational analyses of, in total, seven different IVIM–DTI models with varying tensor contributions to the IVIM component.

---

[*]Additional results, which are not included in Table 2, as reference for comparison with non-IVIM studies: the diffusion coefficients in NAWM, WMH, and GM obtained from the non-IVIM model D_6 are higher at 0.83, 1.38, and 0.84×10^{-3} mm^2/s, respectively. The FA values from model D_6 are lower at 0.43, 0.23, and 0.17, respectively.
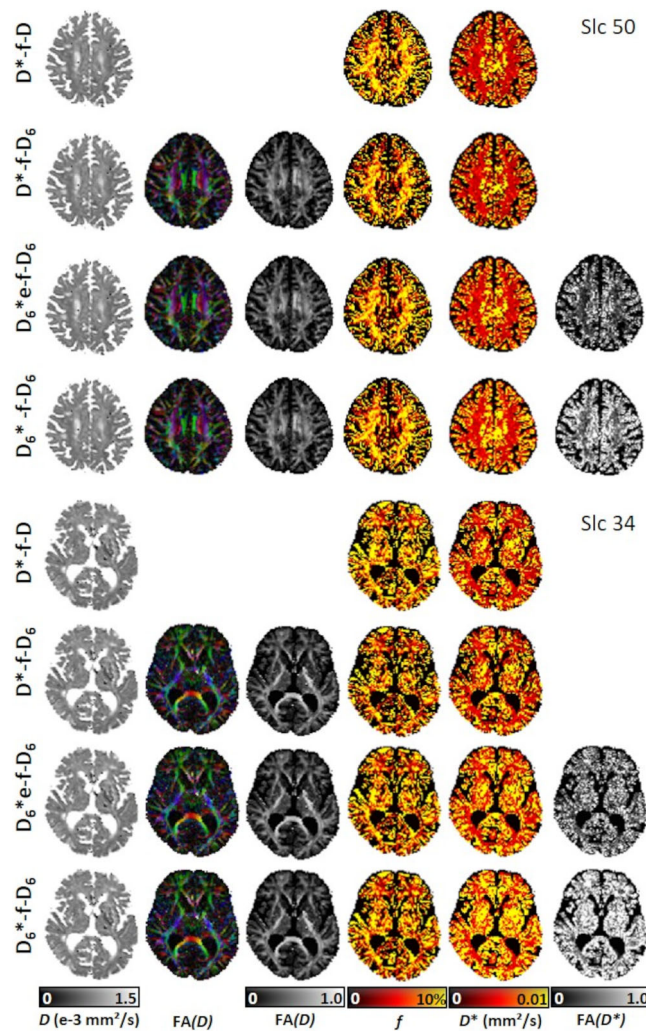
FIGURE 4 Visual comparison of the parameter maps of a participant (74 years old, male) who showed intermediate chi^2 values (i.e., intermediate SNR), determined with four IVIM models (D^*–f–D, D^*–f–D_6, D_6^*e–f–D_6, and D_6^*–f–D_6) for two slice positions. FA maps are displayed for all tensor parameters. In f, D^*, and FA(D^*) maps, CSF voxels are set to 0.
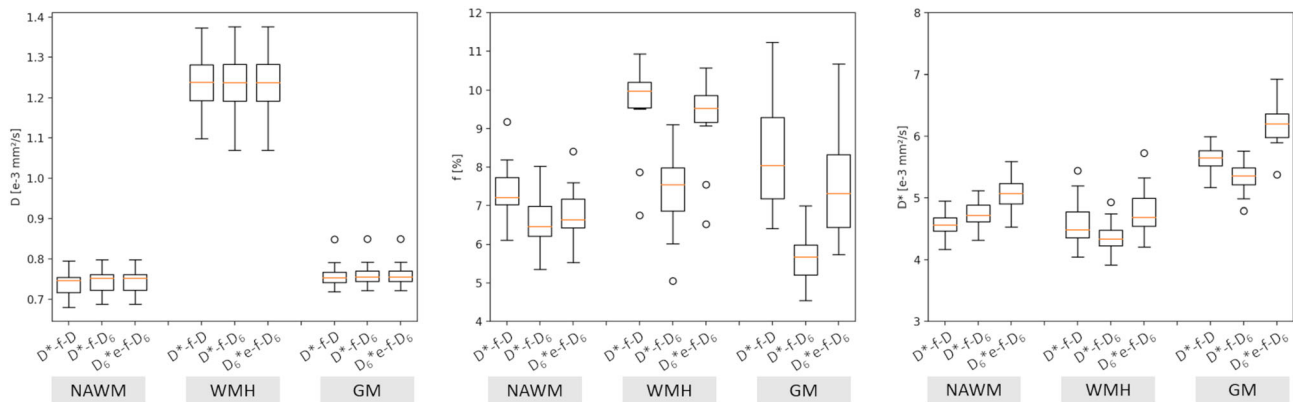

FIGURE 5 Quantitative results for the diffusion coefficient D, perfusion fraction f, and pseudo-diffusion coefficient D^* in NAWM, WMH, and GM obtained with the traditional four-parameter IVIM model (D^*–f–D), the optimal model in NAWM (D^*–f–D_6), and the optimal model in WMH and GM (D_6^*e–f–D_6). The boxplots show the statistical distribution over 20 participants using the individual median values for each tissue.

TABLE 2 Diffusion and IVIM-perfusion parameters in different tissues; median values [interquartile range] over 20 participants

Region	Model	D (10^{-3} mm^2/s)	FA(D)	f (%)	D^* (10^{-3} mm^2/s)	FA(D^*)
NAWM	D^*–f–D	0.746 [0.038]	—	7.21 [0.70]	4.563 [0.213]	—
	D^*–f–D_6	0.752 [0.038]	0.459 [0.029]	6.46 [0.77]	4.719 [0.266]	—
	D_6^*e–f–D_6	0.752 [0.038]	0.459 [0.029]	6.64 [0.75]	5.071 [0.333]	0.445 [0.046]
WMH	D^*–f–D	1.238 [0.089]	—	9.98 [0.66]	4.490 [0.420]	—
	D^*–f–D_6	1.238 [0.091]	0.244 [0.048]	7.54 [1.11]	4.340 [0.255]	—
	D_6^*e–f–D_6	1.238 [0.091]	0.244 [0.048]	9.53 [0.69]	4.691 [0.447]	0.229 [0.062]
GM	D^*–f–D	0.753 [0.026]	—	8.05 [2.11]	5.647 [0.250]	—
	D^*–f–D_6	0.756 [0.026]	0.189 [0.017]	5.67 [0.78]	5.359 [0.276]	—
	D_6^*e–f–D_6	0.756 [0.026]	0.189 [0.017]	7.31 [1.87]	6.202 [0.385]	0.363 [0.047]
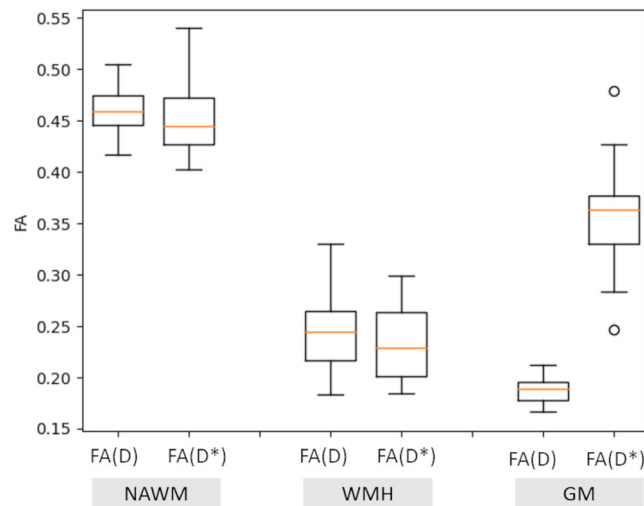
FIGURE 6 FA(D) and FA(D^*) in NAWM, WMH, and GM obtained with the (optimal) model D_6^*e–f–D_6. The boxplots show the statistical distribution over 20 participants using the individual median values in each brain region.

While it is well known that anisotropic diffusion tensors are required to adequately capture water diffusion in the brain, the relevance of tensor-aware IVIM models in the brain (or in most other biological tissues) is less clear. Only a few studies have demonstrated evidence for anisotropic blood flow properties (e.g., in the renal medulla[15,16] or in the liver[7]), and first preliminary evaluations have been published for the human brain.[17,47]

A major challenge in the combined evaluation of conventional diffusion tensors and IVIM-related tensors is the large number of free parameters that must be fitted by such models. Each tensor has six free parameters, so combining a conventional tensor, D, and a pseudo-diffusion tensor, D^*, requires the fit of 12 tensor parameters plus a weighting factor (namely, the perfusion fraction f). Allowing both the pseudo-diffusion coefficient and the perfusion fraction to be described by tensors as proposed by some authors[16,47] would increase this to 18 free tensor parameters (cf. Supporting Information 3 for the evaluation of models with perfusion fraction tensor). In contrast to established two-tensor (or multi-tensor) models that are commonly used to resolve WM fiber crossings,[48] the calculation of additional tensors from the IVIM signal at low b-values is compromised by the inherent general difficulty of biexponential (or multiexponential) fitting in the presence of noise,[13] and by the fact that the IVIM signal effect is relatively small compared with the contribution of the parenchymal diffusion signal. Thus, it is necessary to verify carefully and quantitatively whether the improved fit of IVIM–DTI models with more free parameters can really be attributed to a model that better describes the data, or is only due to noise (over-)fitting.

The expected behavior is that models with more fit parameters show improved goodness of fit, i.e., a reduced sum of squared fit errors (chi^2). This is reflected by our results, which exhibit the smallest chi^2 values (median over all GM or WM voxels) with the most extensive model, D_6^*–f–D_6 (Figure 2), which has $p = 14$ free parameters, followed by the model D_6^*e–f–D_6 with $p = 11$ free parameters. However, the large number of free parameters can result in problems related to overfitting.

The AICc and the derived Akaike weight compensate for the overfitting effect seen with models with many fit parameters and are established metrics to decide if a model really fits better or not.[44] By balancing the goodness of fit (chi^2) and the number of free parameters (p), the highest
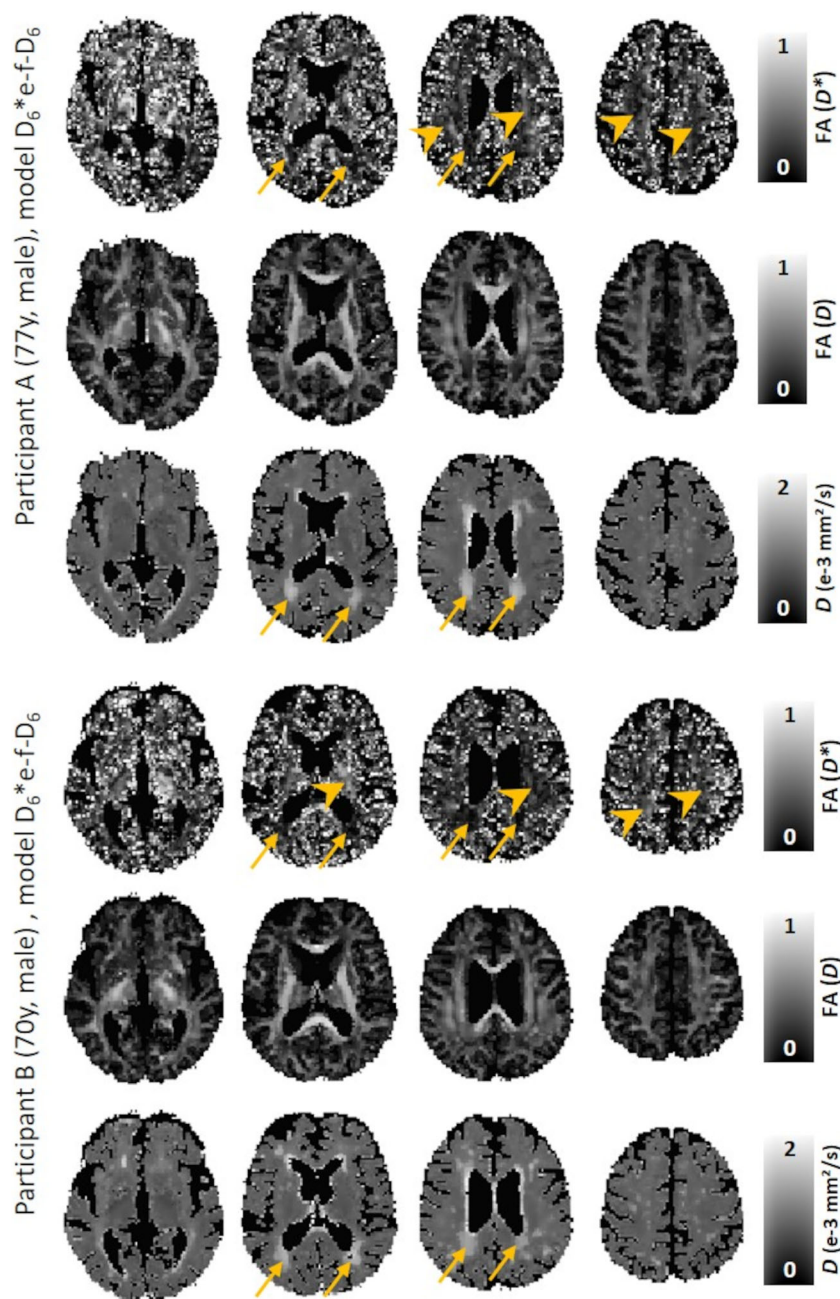
FIGURE 7 FA(D^*) maps (Rows 1 and 4) with corresponding FA(D) maps (Rows 2 and 5) and diffusivity maps (Rows 3 and 6) from two representative participants (A, 77 years old, male; B, 70 years old, male). Shown are four slices (from left to right) of each map; the CSF region has been set to 0. All maps were calculated with the (GM and WMH optimal) model D_6^*e−f−D_6. Areas with hyperintense lesions and low FA(D^*) are indicated by arrows, areas with smoothly distributed FA(D^*) values by arrow heads. (Additional data pre-processing *only* for this visualization: to increase the SNR and obtain smoother visualizations, the diffusion-weighted signal of each voxel was replaced by the mean value of an approximately spherical region around this voxel consisting of a total of 19 voxels (a $3 \times 3 \times 3$ cube without the eight corner voxels); only voxels belonging to the same tissue mask were averaged.)

Akaike weight points to the most adequate model (which, of course, may be different for different tissues or different voxels). In our results, the significantly highest Akaike weights were found for the nine-parameter model D^*−f−D_6 in NAWM and for the 11-parameter model D_6^*e−f−D_6 in WMH and GM (Figure 3). These are biexponential models with a diffusion tensor describing the restricted water diffusion at high b-values (between about 400 and 1000 s/mm^2) and IVIM components describing fast pseudo-diffusion at low b-values (below 400 s/mm^2). This IVIM part is modeled with two scalar parameters in the nine-parameter model D^*−f−D_6, but tensorial in the 11-parameter model D_6^*e−f−D_6. The latter model uses the same eigenvectors for water diffusion (D_6) and pseudo-diffusion (D_6^*), but allows fitting of three optimal eigenvalues for pseudo-diffusion. Thus, the principal axes of the pseudo-diffusion ellipsoid are the same as for tissue diffusion, but the shape and thus anisotropy of this

ellipsoid can be different, which allows for the calculation of the FA of the pseudo-diffusion tensor as a perfusion-related parameter in addition to the magnitude of pseudo-diffusion (D^*). In other words, with the imaging data obtained by the current fast scan protocol we found no evidence for independent orientations of the parenchymal diffusion and the pseudo-diffusion due to the blood microcirculation. This missing evidence, however, is of course no proof or indication that diffusion and pseudo-diffusion tensors are oriented along the same axis. Longer protocols with higher signal-to-noise ratio and/or increased angular resolution might be required to resolve information of the spatial orientation of the blood microcirculation that is independent of the fiber orientation. Generally, very complex models with fully tensorial perfusion properties of the pseudo-diffusion (such as $D_6^*–f–D_6$) can consistently improve the chi^2 values, but not as much as would be required to clearly favor these models in terms of the AICc and Akaike weight.

All models were fitted in a step-wise ("segmented") approach, which required the definition of a threshold b-value b_{segm} to differentiate the fast pseudo-diffusion regime from the slow tissue diffusion regime. The threshold was set to the relatively high value of $b_{segm} = 400$ s/mm^2 in this study, since the pseudo-diffusion coefficients were rather low with values around 5×10^{-3} mm^2/s, which is only approximately eight times the value of the tissue diffusion coefficients. Thus, b-values greater than 400 s/mm^2 are required to suppress the pseudo-diffusion signal component to at most $\exp(-bD^*) \approx \exp(-2) \approx 14\%$ (or less at higher b-values). An additional evaluation with a higher threshold of $b_{segm} = 600$ s/mm^2 is presented in Supporting Information 2. Overall, the results are similar to the ones from the evaluation with a threshold of 400 s/mm^2, although slightly more heterogeneous between participants. The best-performing model (in terms of the Akaike weight) was again $D_6^*e–f–D_6$ in WMH and GM, and this model was now also preferred (in 13 of 20 participants) for NAWM (which is the main difference in model selection results compared with the originally used lower threshold b-value of 400 s/mm^2). However, the chi^2 values were systematically larger with the higher threshold value than with the original one. The latter observation indicates that the evaluation with $b_{segm} = 400$ s/mm^2 may provide a better compromise between regime separation (tissue diffusion versus perfusion) and quality of fit of the tissue diffusion part. From the two favored IVIM–DTI models, conventional DTI parameters such as the FA or main diffusion direction can be extracted and at least two scalar perfusion-related parameters, namely the perfusion fraction, f, and the pseudo-diffusion coefficient, D^*. Apart from providing these tissue parameters, an advantage of a combined isotropic IVIM and DTI analysis is the correction of the DTI parameters: it has been described before by Stieb et al. (and is confirmed by our results) that diffusivity and FA values can be corrected by removing the influence of the perfusion-related signal.[49] As an additional parameter, the perfusion anisotropy, FA(D^*), can be calculated with the model $D_6^*e–f–D_6$, which appears to be slightly lower than FA(D) in WMH, but higher in GM. However, the higher FA(D^*) values in GM may be influenced by noise, which artificially increases the calculated anisotropy values. Studies with better signal-to-noise characteristics (for instance with longer scan protocols) or more participants, including patients and healthy controls, will be required to investigate the clinical and pathophysiological implications of this additional perfusion parameter, which falls outside the scope of this research work.

The quantitative evaluation based on the optimal model yielded results (Table 2) that are mostly consistent with data from earlier studies. Several IVIM results were summarized by Vieni et al. and our results for f are in the rather broad range (2.04% to 14.1%) listed there, while our results for D^* are slightly lower than the values (6.22 to 21 $\times 10^{-3}$ mm^2/s) of that overview.[50] A possible explanation for this discrepancy is that the average age of the study participants listed by Vieni et al. was in most cases considerably lower (distributed around 30 years) than in our study. A recent study by Liao et al. found similar values (within 20%) for f and D^* with their optimal model (however, again in younger participants of 38.3 ± 7.5 years), which resulted in relatively low D^* values as well.[51] Our diffusion coefficients, D, in NAWM and GM agree well with results obtained by Hu et al. (within 10%, but in younger participants) or Wong et al. (within 5%, in elderly participants similar to our cohort).[52,53] Our FA(D) values in WM are compatible with age-dependent reference values by Kochunov et al. for participants with an average age of 77 years.[54] It should be noted that the presented reference values are median values over relatively large tissue regions; further analysis and comparison with a healthy control group is required to analyze potential regional variations in patients relative to controls.

The perfusion fraction, f, in GM (and in WMH) shows an interesting dependence on the IVIM model, with considerably lower values determined with $D^*–f–D_6$ (Table 2 and Figure 5). The higher perfusion fractions obtained with the traditional IVIM model $D^*–f–D$ and with the 11-parameter model $D_6^*e–f–D_6$ appear physiologically plausible. The rather low values obtained with $D^*–f–D_6$ may be explained by the influence of pseudo-diffusion anisotropy: With $D^*–f–D_6$, the scalar values, D^* and f, were fitted to the individual signals from all gradient directions and b-values (Equation 4), which is equivalent to taking the *arithmetic* mean value of the signals over all gradient directions. However, to obtain correct tensor-trace values, either the *geometric* mean value of the signal intensities should be used (as in $D^*–f–D$) or a tensor should be fitted (as in $D_6^*e–f–D_6$). Therefore, one may assume that the model $D_6^*e–f–D_6$ results in corrected and more realistic values of D^* than $D^*–f–D_6$ and, consequently, also in corrected values of f. However, without more reliable reference values for the perfusion fraction, the interpretation of these differences remains speculative.

This study has some limitations. First, many more IVIM–DTI models could be considered for data analysis (e.g., using four-parameter instead of six-parameter tensors[55]). In addition, we restricted IVIM fitting to a simple step-wise ("segmented") algorithm with a fixed threshold to differentiate between slow and fast diffusion components. Other approaches such as Bayesian fitting, full bi-exponential fitting, or deep-learning-based fitting[56–58] are available but are beyond the scope of this work. Furthermore, extensions of scalar models have also successfully been applied, in which the faster diffusion regime (i.e. lower b-values) is modeled by two (spectral) diffusion components in patients with cerebrovascular pathology, one for the blood microcirculation and one component thought to represent interstitial fluid.[29,59]

Second, our model-selection results must be expected to depend strongly on the data quality, i.e. in particular on the signal-to-noise ratio and number of b-values and diffusion-gradient directions. With substantially higher SNR, more parameters (as in the $D_6^*-f-D_6$ model) might be accurately measurable; however, this would require much longer scan durations. The publications by Finkenstaedt et al. and Mozumder et al.[17,47] used substantially longer IVIM–DTI protocols with scan times of about 30 min to assess tensor properties of the pseudo-diffusion and of the perfusion fraction in the brain. They presented promising results, but did not perform any model selection analysis with statistical methods such as the Akaike or the Bayesian information criterion. In the present study, we used a protocol with a clinically feasible scan duration of 5 min 21 s. This had the advantage that scans could be performed in a large cohort of participants with clinically relevant pathologies. Any potential overfitting of our data with models with too many degrees of freedom was controlled by strict model selection based on the AICc. With respect to the available signal-to-noise ratio, it should also be noted that our protocol acquired relatively thin slices with cubic $2 \times 2 \times 2$ mm^3 voxels, which is typical for DTI applications, while many (scalar) IVIM protocols acquire much thicker slices resulting in higher SNR, but anisotropic voxel dimensions and more severe partial volume effects.

Third, one could argue that a region-based, in contrast to a voxel-based, approach would be more adequate to tackle the relatively low signal-to-noise ratio due to the small perfusion signal effect in the IVIM models. However, as the investigated patients displayed regional brain tissue inhomogeneities, for instance WMH, and region-based approaches generally average over a distribution of different tensor orientations, we feel that the voxel-based approach is well justified.

Finally, considering the quantitative IVIM and diffusion parameters obtained, we acknowledge that these values may be influenced by the presence of cSVD in the participants and are not necessarily identical to parameters in younger or age-matched healthy controls. However, analyzing data from this cohort had the advantage that the clinical feasibility of the acquisition protocol and influence of, e.g., motion artifacts are more realistically represented than in young healthy controls. By establishing the method in the target population, not in healthy volunteers, we ensure applicability for clinical use.

Currently, there is no effective treatment for cSVD and its progression over time is hard to predict. Clinical progress in this field relies on better understanding of the pathophysiological mechanisms underlying this disease. The clinical value of establishing such complex mathematical models for MRI in patients with cSVD is that we can capture both abnormalities of the parenchyma and blood microcirculation within one time-efficient MRI scan, and describe microstructural tissue and blood circulation parameters in a physiological/physical and quantitative way, more accurately than with purely scalar models. This is relevant from a logistic point of view, as most clinical research neuroimaging protocols are constituted of multiple sequences and often need to be integrated in clinical MRI slots with limited time. Finally, cSVD is a brain disorder in which cerebrovascular pathology interacts with the neural tissue, for which an integral approach of the brain parenchyma and microcirculation is most pathophysiologically adequate. Future studies need to show whether advanced tensor IVIM models can provide distinct parameters that discern normal from affected tissue parts and add to scalar models, which was beyond the current study scope.

In conclusion, using a short (5 min 21 s) integrated IVIM–DTI protocol with 15 b-values and six diffusion directions for each b-value we demonstrate that IVIM models with 9 and 11 parameters were most adequate to simultaneously determine parameters such as perfusion fraction, f, and pseudo-diffusion coefficient, D^*, as well as DTI parameters. The (11-parameter) model with the highest Akaike weights in WMH and GM allowed for the additional calculation of the FA of the pseudo-diffusion tensor, which is not accessible with the usually performed IVIM acquisitions based on three orthogonal diffusion-gradient directions.

ACKNOWLEDGEMENTS

CODE AVAILABILITY

The code of the IVIM-DTI models is available at https://github.com/o-dietrich/ivimdti-models.

ORCID

Olaf Dietrich https://orcid.org/0000-0001-6182-5039

REFERENCES

1. Le Bihan D, Breton E, Lallemand D, Aubin ML, Vignaud J, Laval-Jeantet M. Separation of diffusion and perfusion in intravoxel incoherent motion MR imaging. *Radiology*. 1988;168(2):497-505. doi:10.1148/radiology.168.2.3393671
2. Le Bihan D, Breton E, Lallemand D, Grenier P, Cabanis E, Laval-Jeantet M. MR imaging of intravoxel incoherent motions: application to diffusion and perfusion in neurologic disorders. *Radiology*. 1986;161(2):401-407. doi:10.1148/radiology.161.2.3763909
3. Basser PJ, Mattiello J, LeBihan D. Estimation of the effective self-diffusion tensor from the NMR spin echo. *J Magn Reson B*. 1994;103(3):247-254. doi:10.1006/jmrb.1994.1037
4. Pierpaoli C, Jezzard P, Basser PJ, Barnett A, Di Chiro G. Diffusion tensor MR imaging of the human brain. *Radiology*. 1996;201(3):637-648. doi:10.1148/radiology.201.3.8939209

5. Konieczny MJ, Dewenter A, Ter Telgte A, et al. Multi-shell diffusion MRI models for white matter characterization in cerebral small vessel disease. *Neurology*. 2021;96(5):e698-e708. doi:10.1212/WNL.0000000000011213

6. Lee MB, Kim YH, Jahng GH, Kwon OI. Angular resolution enhancement technique for diffusion-weighted imaging (DWI) using predicted diffusion gradient directions. *Neuroimage*. 2018;183:836-846. doi:10.1016/j.neuroimage.2018.08.072

7. Phi van V, Reiner CS, Klarhoefer M, et al. Diffusion tensor imaging of the abdominal organs: influence of oriented intravoxel flow compartments. *NMR Biomed*. 2019;32(11):e4159. doi:10.1002/nbm.4159

8. Le Bihan D. What can we see with IVIM MRI? *Neuroimage*. 2019;187:56-67. doi:10.1016/j.neuroimage.2017.12.062

9. Federau C. Intravoxel incoherent motion MRI as a means to measure in vivo perfusion: a review of the evidence. *NMR Biomed*. 2017;30(11):e3780. doi:10.1002/nbm.3780

10. Schneider MJ, Dietrich O, Ingrisch M, et al. Intravoxel incoherent motion magnetic resonance imaging in partially nephrectomized kidneys. *Invest Radiol*. 2016;51(5):323-330. doi:10.1097/RLI.0000000000000244

11. Schneider MJ, Gaass T, Ricke J, Dinkel J, Dietrich O. Assessment of intravoxel incoherent motion MRI with an artificial capillary network: analysis of biexponential and phase-distribution models. *Magn Reson Med*. 2019;82(4):1373-1384. doi:10.1002/mrm.27816

12. Thoeny HC, Zumstein D, Simon-Zoula S, et al. Functional evaluation of transplanted kidneys with diffusion-weighted and BOLD MR imaging: initial experience. *Radiology*. 2006;241(3):812-821. doi:10.1148/radiol.2413060103

13. De Groen PDM, De Moor B. The fit of a sum of exponentials to noisy data. *J Comput Appl Math*. 1987;20:175-187. doi:10.1016/0377-0427(87)90135-X

14. Federau C, O'Brien K, Meuli R, Hagmann P, Maeder P. Measuring brain perfusion with intravoxel incoherent motion (IVIM): initial clinical experience. *J Magn Reson Imaging*. 2014;39(3):624-632. doi:10.1002/jmri.24195

15. Notohamiprodjo M, Chandarana H, Mikheev A, et al. Combined intravoxel incoherent motion and diffusion tensor imaging of renal diffusion and flow anisotropy. *Magn Reson Med*. 2015;73(4):1526-1532. doi:10.1002/mrm.25245

16. Hilbert F, Bock M, Neubauer H, et al. An intravoxel oriented flow model for diffusion-weighted imaging of the kidney. *NMR Biomed*. 2016;29(10):1403-1413. doi:10.1002/nbm.3584

17. Mozumder M, Beltrachini L, Collier Q, Pozo JM, Frangi AF. Simultaneous magnetic resonance diffusion and pseudo-diffusion tensor imaging. *Magn Reson Med*. 2018;79(4):2367-2378. doi:10.1002/mrm.26840

18. Paschoal AM, Secchinatto KF, da Silva PHR, et al. Contrast-agent-free state-of-the-art MRI on cerebral small vessel disease-part 1. ASL, IVIM, and CVR. *NMR Biomed*. 2022;35(8):e4742. doi:10.1002/nbm.4742

19. da Silva PHR, Paschoal AM, Secchinatto KF, et al. Contrast agent-free state-of-the-art magnetic resonance imaging on cerebral small vessel disease—part 2: Diffusion tensor imaging and functional magnetic resonance imaging. *NMR Biomed*. 2022;35(8):e4743. doi:10.1002/nbm.4743

20. Ter Telgte A, van Leijsen EMC, Wiegertjes K, Klijn CJM, Tuladhar AM, de Leeuw FE. Cerebral small vessel disease: from a focal to a global perspective. *Nat Rev Neurol*. 2018;14(7):387-398. doi:10.1038/s41582-018-0014-y

21. Wardlaw JM, Smith EE, Biessels GJ, et al. Neuroimaging standards for research into small vessel disease and its contribution to ageing and neurodegeneration. *Lancet Neurol*. 2013;12(8):822-838. doi:10.1016/S1474-4422(13)70124-8

22. Pantoni L, Gorelick PB (Eds). *Cerebral Small Vessel Disease*. Cambridge University Press; 2014. doi:10.1017/CBO9781139382694

23. Markus HS, Lythgoe DJ, Ostegaard L, O'Sullivan M, Williams SC. Reduced cerebral blood flow in white matter in ischaemic leukoaraiosis demonstrated using quantitative exogenous contrast based perfusion MRI. *J Neurol Neurosurg Psychiatry*. 2000;69(1):48-53. doi:10.1136/jnnp.69.1.48

24. O'Sullivan M, Lythgoe DJ, Pereira AC, et al. Patterns of cerebral blood flow reduction in patients with ischemic leukoaraiosis. *Neurology*. 2002;59(3):321-326. doi:10.1212/wnl.59.3.321

25. Shi Y, Thrippleton MJ, Makin SD, et al. Cerebral blood flow in small vessel disease: a systematic review and meta-analysis. *J Cereb Blood Flow Metab*. 2016;36(10):1653-1667. doi:10.1177/0271678X16662891

26. Tuladhar AM, van Norden AG, de Laat KF, et al. White matter integrity in small vessel disease is related to cognition. *NeuroImage Clin*. 2015;7:518-524. doi:10.1016/j.nicl.2015.02.003

27. de Laat KF, Tuladhar AM, van Norden AG, Norris DG, Zwiers MP, de Leeuw FE. Loss of white matter integrity is associated with gait disorders in cerebral small vessel disease. *Brain*. 2011;134(Pt 1):73-83. doi:10.1093/brain/awq343

28. Wong SM, Zhang CE, van Bussel FC, et al. Simultaneous investigation of microvasculature and parenchyma in cerebral small vessel disease using intravoxel incoherent motion imaging. *NeuroImage Clin*. 2017;14:216-221. doi:10.1016/j.nicl.2017.01.017

29. van der Thiel MM, Freeze WM, Verheggen ICM, et al. Associations of increased interstitial fluid with vascular and neurodegenerative abnormalities in a memory clinic sample. *Neurobiol Aging*. 2021;106:257-267. doi:10.1016/j.neurobiolaging.2021.06.017

30. van Leijsen EMC, van Uden IWM, Ghafoorian M, et al. Nonlinear temporal dynamics of cerebral small vessel disease: the RUN DMC study. *Neurology*. 2017;89(15):1569-1577. doi:10.1212/WNL.0000000000004490

31. Cai M, Jacob MA, van Loenen MR, et al. Determinants and temporal dynamics of cerebral small vessel disease: 14-year follow-up. *Stroke*. 2022;53(9):2789-2798. doi:10.1161/STROKEAHA.121.038099

32. Feinberg DA, Moeller S, Smith SM, et al. Multiplexed echo planar imaging for sub-second whole brain FMRI and fast diffusion imaging. *PLoS ONE*. 2010;5(12):e15710. doi:10.1371/journal.pone.0015710

33. Moeller S, Yacoub E, Olman CA, et al. Multiband multislice GE-EPI at 7 tesla, with 16-fold acceleration using partial parallel imaging with application to high spatial and temporal whole-brain fMRI. *Magn Reson Med*. 2010;63(5):1144-1153. doi:10.1002/mrm.22361

34. Xu J, Moeller S, Auerbach EJ, et al. Evaluation of slice accelerations using multiband echo planar imaging at 3 T. *Neuroimage*. 2013;83:991-1001. doi:10.1016/j.neuroimage.2013.07.055

35. O'Brien KR, Kober T, Hagmann P, et al. Robust T_1-weighted structural brain imaging and morphometry at 7T using MP2RAGE. *PLoS ONE*. 2014;9(6):e99676. doi:10.1371/journal.pone.0099676

36. Long J, Shelhamer E, Darrell T. Fully convolutional networks for semantic segmentation. *Proc IEEE Comput Soc Conf Comput Vis Pattern Recognit*. 2015;3431-3440. doi:10.1109/CVPR.2015.7298965

37. Puonti O, Iglesias JE, Van Leemput K. Fast and sequence-adaptive whole-brain segmentation using parametric Bayesian modeling. *Neuroimage*. 2016;143:235-249. doi:10.1016/j.neuroimage.2016.09.011

38. Avants BB, Tustison NJ, Song G, Cook PA, Klein A, Gee JC. A reproducible evaluation of ANTs similarity metric performance in brain image registration. *Neuroimage*. 2011;54(3):2033-2044. doi:10.1016/j.neuroimage.2010.09.025

39. Tournier JD, Smith R, Raffelt D, et al. MRtrix3: a fast, flexible and open software framework for medical image processing and visualisation. *Neuroimage*. 2019;202:116137. doi:10.1016/j.neuroimage.2019.116137

40. Andersson JL, Skare S, Ashburner J. How to correct susceptibility distortions in spin-echo echo-planar images: application to diffusion tensor imaging. *Neuroimage*. 2003;20(2):870-888. doi:10.1016/S1053-8119(03)00336-7

41. Andersson JLR, Sotiropoulos SN. An integrated approach to correction for off-resonance effects and subject movement in diffusion MR imaging. *Neuroimage*. 2016;125:1063-1078. doi:10.1016/j.neuroimage.2015.10.019

42. Terlouw JPV, Vogelaar MG. *Kapteyn Package. Version 2.3b3*. Kapteyn Astronomical Institute; 2014.

43. Akaike H. A new look at the statistical model identification. *IEEE Trans Autom Control*. 1974;19(6):716-723. doi:10.1109/TAC.1974.1100705

44. Glatting G, Kletting P, Reske SN, Hohl K, Ring C. Choosing the optimal fit function: comparison of the Akaike information criterion and the *F*-test. *Med Phys*. 2007;34(11):4285-4292. doi:10.1118/1.2794176

45. Burnham KP, Anderson DR. Multimodel inference: understanding AIC and BIC in model selection. *Sociol Method Res*. 2004;33(2):261-304. doi:10.1177/0049124104268644

46. James G, Witten D, Hastie T, Tibshirani R. *An Introduction to Statistical Learning with Applications in R*. Springer; 2021. doi:10.1007/978-1-0716-1418-1

47. Finkenstaedt T, Klarhoefer M, Eberhardt C, et al. The IVIM signal in the healthy cerebral gray matter: a play of spherical and non-spherical components. *Neuroimage*. 2017;152:340-347. doi:10.1016/j.neuroimage.2017.03.004

48. Ozarslan E, Mareci TH. Generalized diffusion tensor imaging and analytical relationships between diffusion tensor imaging and high angular resolution diffusion imaging. *Magn Reson Med*. 2003;50(5):955-965. doi:10.1002/mrm.10596

49. Stieb S, Klarhoefer M, Finkenstaedt T, et al. Correction for fast pseudo-diffusive fluid motion contaminations in diffusion tensor imaging. *Magn Reson Imaging*. 2020;66:50-56. doi:10.1016/j.mri.2019.09.009

50. Vieni C, Ades-Aron B, Conti B, et al. Effect of intravoxel incoherent motion on diffusion parameters in normal brain. *Neuroimage*. 2020;204:116228. doi:10.1016/j.neuroimage.2019.116228

51. Liao YP, Urayama SI, Isa T, Fukuyama H. Optimal model mapping for intravoxel incoherent motion MRI. *Front Hum Neurosci*. 2021;15:617152. doi:10.3389/fnhum.2021.617152

52. Hu YC, Yan LF, Han Y, et al. Can the low and high *b*-value distribution influence the pseudodiffusion parameter derived from IVIM DWI in normal brain? *BMC Med Imaging*. 2020;20(1):14. doi:10.1186/s12880-020-0419-0

53. Wong SM, Backes WH, Zhang CE, et al. On the reproducibility of inversion recovery intravoxel incoherent motion imaging in cerebrovascular disease. *Am J Neuroradiol*. 2018;39(2):226-231. doi:10.3174/ajnr.A5474

54. Kochunov P, Glahn DC, Lancaster J, et al. Fractional anisotropy of cerebral white matter and thickness of cortical gray matter across the lifespan. *Neuroimage*. 2011;58(1):41-49. doi:10.1016/j.neuroimage.2011.05.050

55. Ferizi U, Ruiz A, Rossi I, Bencardino J, Raya JG. A robust diffusion tensor model for clinical applications of MRI to cartilage. *Magn Reson Med*. 2018;79(2):1157-1164. doi:10.1002/mrm.26702

56. Barbieri S, Gurney-Champion OJ, Klaassen R, Thoeny HC. Deep learning how to fit an intravoxel incoherent motion model to diffusion-weighted MRI. *Magn Reson Med*. 2020;83(1):312-321. doi:10.1002/mrm.27910

57. Barbieri S, Donati OF, Froehlich JM, Thoeny HC. Comparison of intravoxel incoherent motion parameters across MR imagers and field strengths: evaluation in upper abdominal organs. *Radiology*. 2016;279(3):784-794. doi:10.1148/radiol.2015151244

58. Neil JJ, Bretthorst GL. On the use of Bayesian probability theory for analysis of exponential decay data: an example taken from intravoxel incoherent motion experiments. *Magn Reson Med*. 1993;29(5):642-647. doi:10.1002/mrm.1910290510

59. Wong SM, Backes WH, Drenthen GS, et al. Spectral diffusion analysis of intravoxel incoherent motion MRI in cerebral small vessel disease. *J Magn Reson Imaging*. 2020;51(4):1170-1180. doi:10.1002/jmri.26920

SUPPORTING INFORMATION

Additional supporting information can be found online in the Supporting Information section at the end of this article.